Measurement of differential and angle-integrated cross sections for the $^{10}B(n, \alpha)^7Li$ reaction from 0.3 eV to 3.0 MeV at CSNS Back-n*

Wenkai Ren (任文凯)[1] Han Yi (易晗)[2,3] Haofan Bai (白浩帆)[1] Jie Liu (刘杰)[1] Kang Sun (孙康)[2,3] Wei Jiang (蒋伟)[2,3] Zepeng Wu (邬泽鹏)[1] Cong Xia (夏聪)[1] Guohui Zhang (张国辉)[1†] Yonghao Chen (陈永浩)[2,3] Ruirui Fan (樊瑞睿)[2,3] Qiwen Fan (樊启文)[4] Shixiang Peng (彭士香)[1] Wentian Cao (曹文田)[1] Tieshuan Fan (樊铁栓)[1]

[1]State Key Laboratory of Nuclear Physics and Technology, Institute of Heavy Ion Physics, Peking University, Beijing 100871, China
[2]Institute of High Energy Physics, Chinese Academy of Sciences, Beijing 100049, China
[3]Spallation Neutron Source Science Center, Dongguan 523803, China
[4]China Institute of Atomic Energy, Beijing 102413, China

Abstract: In the present study, new measurements of differential and angle-integrated cross sections for the $^{10}B(n, \alpha_1)^7Li^*$, $^{10}B(n, \alpha_0)^7Li$, and $^{10}B(n, \alpha)^7Li$ reactions were performed at the CSNS Back-n white neutron source. The Light-charged Particle Detector Array (LPDA) system was used to detect charged particles. The ^6Li-Si monitor was employed to measure the neutron flux. The differential cross sections for the $^{10}B(n, \alpha)^7Li$ reaction were obtained from 20.1° to 158.3° (13 angles) in the neutron energy region from 0.3 eV to 3.0 MeV (70 energy points). The differential cross sections for the $^{10}B(n, \alpha_0)^7Li$ and $^{10}B(n, \alpha_1)^7Li^*$ reactions were also obtained at the same angular positions in the neutron energy region from 0.3 eV to 1.0 MeV (65 energy points). Fitting with the Legendre polynomial series, the angle-integrated cross sections of these three reactions were obtained through integration. The experimental data for these three reactions across such a wide neutron energy range are valuable references for future nuclear data evaluations.

Keywords: $^{10}B(n, \alpha)^7Li$, differential cross section, angle-integrated cross section, nuclear data

DOI: 10.1088/1674-1137/ae5dae **CSTR:** 32044.14.ChinesePhysicsC.50074001

I. INTRODUCTION

The neutron induced ^{10}B reaction is one of the most important reactions in nuclear engineering, which includes neutron detection, reactor control, and boron neutron capture therapy (BNCT). [1]. In addition, the study of the $n + {}^{10}B$ system can enhance our understanding of nuclear reaction mechanism in light nuclei [2]. In the neutron energy region below 1 MeV, the $^{10}B(n, \alpha)^7Li$ reaction is dominant among neutron induced ^{10}B reactions, which can be further divided into $^{10}B(n, \alpha_0)^7Li$ ($Q = 2.79$ MeV) and $^{10}B(n, \alpha_1)^7Li^*$ ($Q = 2.31$ MeV) reactions, corresponding to the ground state and the first excited state of the residual nuclei ^7Li. In the neutron energy region from thermal to 1 MeV, the cross sections of the $^{10}B(n, \alpha)^7Li$ and $^{10}B(n, \alpha_1)^7Li^*$ reactions have been adopted as standard cross sections [3]. However, in the MeV energy region and above, discrepancies exist among different measurements and evaluations because of the small cross sections, strong background interference, and mutual interference between the $^{10}B(n, \alpha_0)^7Li$ and $^{10}B(n, \alpha_1)^7Li^*$ reactions. Accurate differential cross-section data are essential for nuclear technology applications. Therefore, high-precision measurements are required.

For neutron energy $E_n \leq 1.0$ MeV, although numerous measurements of the $^{10}B(n, \alpha)^7Li$ reaction have been conducted since 1954 [4], only four measurements of angular distribution and differential cross sections (*i.e.*, Sealock [5], Stelts [6], Hambsch [2], and Jiang [7]) can be found in EXFOR [4]; for $1.0 < E_n \leq 3.0$ MeV, only two measurements of differential cross sections (Haoyu Jiang [7] and T.N.Massey [8]) can be found in EXFOR for this reaction [4]. In 2019, our team (Jiang *et al.* [7]) published the differential and angle-integrated cross sections of the $^{10}B(n, \alpha)^7Li$ reaction for the neutron energy range from 1.0 eV to 2.5 MeV, measured at the China Spallation Neutron Source (CSNS) [9] Back streaming

Received 10 February 2026; Accepted 8 April 2026; Accepted manuscript online 9 April 2026

* This work was supported by the National Natural Science Foundation of China (12475299) and the Key Laboratory of Nuclear Data foundation (JCKY2025201C153)

† E-mail: guohuizhang@pku.edu.cn

white neutron source (Back-n) [10, 11]. The measurement used 15 silicon detectors with angle positions ranging from 19.2° to 160.8° to detect charged particles. Under the same experimental conditions, our team (Bai *et al.* [12]) have also measured differential and angle-integrated cross sections of the ^{6}Li(n, t)^{4}He reaction, which have been used in the evaluations of standard cross sections. To reduce the uncertainties introduced from the neutron flux, our team (Liu *et al.* [13]) reanalyzed the measurement data and obtained the ratios of the differential and angle-integrated cross sections of the ^{10}B(n, α)^{7}Li reaction over the ^{6}Li(n, t)^{4}He reaction. Analysis shows that the relative uncertainties of these ratios are primarily attributed to the uncertainties in the results of the ^{10}B(n, α)^{7}Li reaction. Considering these factors, new and accurate measurements of differential and angle-integrated cross sections for the ^{10}B(n, α)^{7}Li reaction are necessary.

In the present study, new measurements of relative differential and angle-integrated cross sections were performed for the ^{10}B(n, α_1)^{7}Li*, ^{10}B(n, α_0)^{7}Li, and ^{10}B(n, α)^{7}Li reactions at CSNS Back-n white neutron source with optimized experimental conditions including thinner samples, thinner backing, stronger neutron fluences, and simultaneous monitoring of the neutron flux using the ^{6}Li(n, t)^{4}He reaction. In the remaining part of this paper, Section II briefly introduces the experimental setup, Section III presents the data analysis processes, and Section IV reports the results and conclusions.

II. EXPERIMENTAL SETUP

The experiment was performed at EndStation#1 of the CSNS Back-n white neutron source in 2024. As shown in Fig. 1, the setup includes three components: the neutron source, the ^{10}B samples, and the charged particle detectors (including the ^{6}Li-Si monitor and the Light-charged Particle Detector Array (LPDA) system).

A. Neutron source

The CSNS Back-n white neutrons were generated using a proton beam (1.6 GeV) bombarding a tungsten target, with neutron energy range spanning from 0.3 eV to 300 MeV [11]. The repetition rate of the beam pulse was 25 Hz, the full width at half maximum (FWHM) was ~70 ns, and the interval between the double proton bunches was 410 ns [14]. During the present experiment, the beam power was ~ 160 kW. The flight path from the spallation target to the samples was 57.99 m. In the EndStation#1 of the CSNS Back-n white neutron source, there are three configuration of the shutter and the Collimator-1. To achieve a balance between high count rates and low background interference, the intermediate configuration of Ø50 mm (shutter) + Ø15 mm (collimator 1) [15] was selected. In contrast to the largest (Ø50 mm (shutter) + Ø50 mm (collimator 1)) and smallest (Ø12 mm (shutter) + Ø15 mm (collimator 1)) configurations, this intermediate setup is less commonly used, and its neutron flux data have not been previously published. For this configuration, the neutron beam spot size was approximately 22 mm. Since the present measurement was performed in the double-bunch mode [16], the unfolding process is necessary in the data analysis.

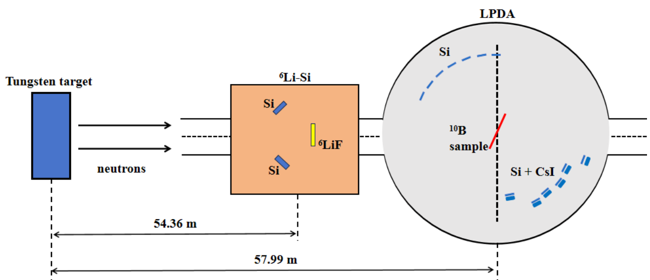

Fig. 1. (color online) The sketch of the experimental setup.

B. Samples

Two enriched (90%) ^{10}B samples were used back-to-back, plated on an aluminum backing with a thickness of 10 μm. The sample data are presented in Table 1, and the corresponding images are shown in Fig. 2. In addition, a 10 μm thick aluminum sheet without samples was used for background measurements. The LPDA sample holder had four sample positions. The ^{241}Am α sources (for energy calibration of the detection system), the ^{10}B samples, and the aluminum sheet were installed at different sample positions [7].

Table 1. Sample characteristics.

Sample position	Sample	Thickness/(μg·cm^{-2})	Diameter/mm
Forward	^{10}B	69.5	50
Backward	^{10}B	73.0	50

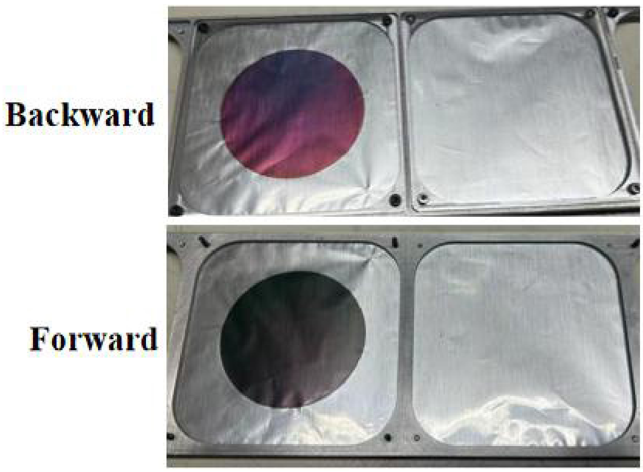

Fig. 2. (color online) Images of the ^{10}B samples.

C. Charged particle detectors and data acquisition system

As shown in Fig. 1, a ^{6}Li-Si [17] monitor (an array of silicon detectors and a ^{6}LiF sample) inside the neutron tube was used to measure the relative neutron flux through the ^{6}Li(n, t)^{4}He reaction. A ^{6}LiF sample (~350 μg/cm^2 thick, ~90% enrichment, 60 mm diameter) deposited on a 10 μm thick aluminum backing film was used. The neutron attenuation of the aluminum backing film was less than 0.15% [17]. The ^{6}Li-Si monitor consisted of the ^{6}LiF sample and the 8 silicon detectors, each with a thickness of 300 μm and a sensitive area of 20 mm × 20 mm. The eight silicon detectors were isotropically distributed around the ^{6}LiF sample at 135° relative to the beam direction.

The Light-charged Particle Detector Array (LPDA) system [18] was used to detect charged particles, as shown in Fig. 1. In the present work, 13 individual silicon detectors (25 mm × 25 mm × 300 μm) were utilized, comprising six forward detectors and seven backward detectors, to cover the particle emission angle from 20.1° to 158.3°. In addition, six cesium iodide scintillator (CsI(Tl)) detectors were installed behind the six forward silicon detectors for measuring the events of the ^{10}B(n, $t2\alpha$) reaction. The distributions of the receiving angles of the 13 silicon detectors with respect to the ^{10}B samples are shown in Fig. 3, and their solid angles are (0.00792 ~ 0.0289) sr according to Monte Carlo simulations using Geant4 code [19]. The uncertainties of the receiving angles were obtained by fitting each curve with a Gaussian function. Signals from the ^{6}Li-Si monitor and LPDA detectors were delivered to the Back-n general purpose data acquisition system (DAQ) [20].

In the present experiment, the ^{10}B samples and the aluminum backing sheet were measured alternately, and the ratio of their measurement durations was approximately 3:1. The beam duration for each turn was ~24 h, and the total beam duration was ~ 240 h.

III. DATA ANALYSIS

The differential cross sections of the ^{10}B(n, α)^{7}Li reaction can be calculated as follows:

$$\frac{d\sigma}{d\Omega}(E_n,\theta_{\rm lab}) = \varepsilon_{\rm nor}\cdot\frac{d\sigma}{d\Omega}(E_n,\theta_{\rm lab})_{\rm realtive} = \varepsilon_{\rm nor}\cdot\frac{N_\alpha(E_n,\theta_{\rm lab})}{I(E_n)\cdot N_{\rm c}\cdot\Delta\Omega\cdot\varepsilon_{\rm d}}, \quad (1)$$

where E_n is the neutron energy, $\theta_{\rm lab}$ is the emission angle of the α particle in the laboratory reference system, $N_\alpha(E_n, \theta_{\rm lab})$ is the α particle count in an energy bin centered at E_n and in the angle bin centered at $\theta_{\rm lab}$, $I(E_n)$ is the relative neutron fluence in each neutron energy bin, $N_{\rm c}$ is the ^{10}B atom number in the sample, $\Delta\Omega$ is the solid angle of each silicon detector in the LPDA, and $\varepsilon_{\rm d}$ is the detection efficiency of each silicon detector. Owing to the lack of an absolute neutron fluence and the non-uniformity correction of the neutron beam, the normalization factor ($\varepsilon_{\rm nor}$) was determined in the neutron energy range from 0.5 eV to 1.5 eV, based on the evaluated data from IAEA-Std17 [3], which is consistent with the values reported in ENDF-B/VIII.1 [21].

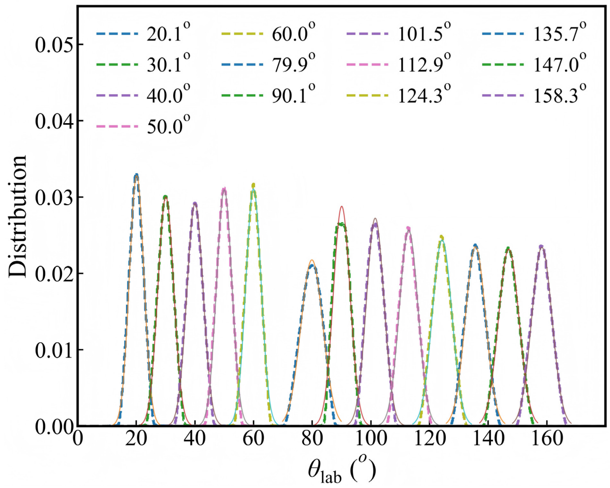

Fig. 3. (color online) Simulated distributions of the receiving angles of the silicon detectors.

The values of $\theta_{\rm lab}$ and $\Delta\Omega$ were obtained in Sec. II.C, and the ^{10}B atom number $N_{\rm c}$ can be calculated from the data presented in Table 1. The value for E_n was determined using the time-of-flight (TOF) method. The uncertainty of E_n was mainly attributed to the width of the proton beam pulse. $N_\alpha(E_n, \theta_{\rm lab})$ was obtained by analyzing the measured LPDA data from the ^{10}B samples, which will be shown in Sec. III.A. The values of $\varepsilon_{\rm d}$ were determined based on a comparison between the measured and simulated spectra. $I(E_n)$ was obtained by analyzing the data from the ^{6}Li-Si monitor. In the present study, relative differential cross sections were obtained, and the relative angle-integrated cross sections were then calculated using Legendre polynomial fitting. Finally, the normalization factor ($\varepsilon_{\rm nor}$) was calculated using the standard cross sections of the ^{10}B(n, α)^{7}Li reaction in the 0.5 ~ 1.5 eV region.

A. Determination of the numbers of the ^{10}B(n, α)^{7}Li, ^{10}B(n, α_0)^{7}Li and ^{10}B(n, α_1)^{7}Li* events

A typical E_n-Amplitude (the amplitude of the signal from the Si detectors) two-dimensional spectrum at 30.1° is shown in Fig. 4(a), where the α_0, α_1, and ^{7}Li events are evident. The simulated E_n-Amplitude two-dimensional spectrum at the same angle position is shown in Fig. 4 (b). The simulation was performed using Geant4 code [19], and 7 reaction channels were considered, including

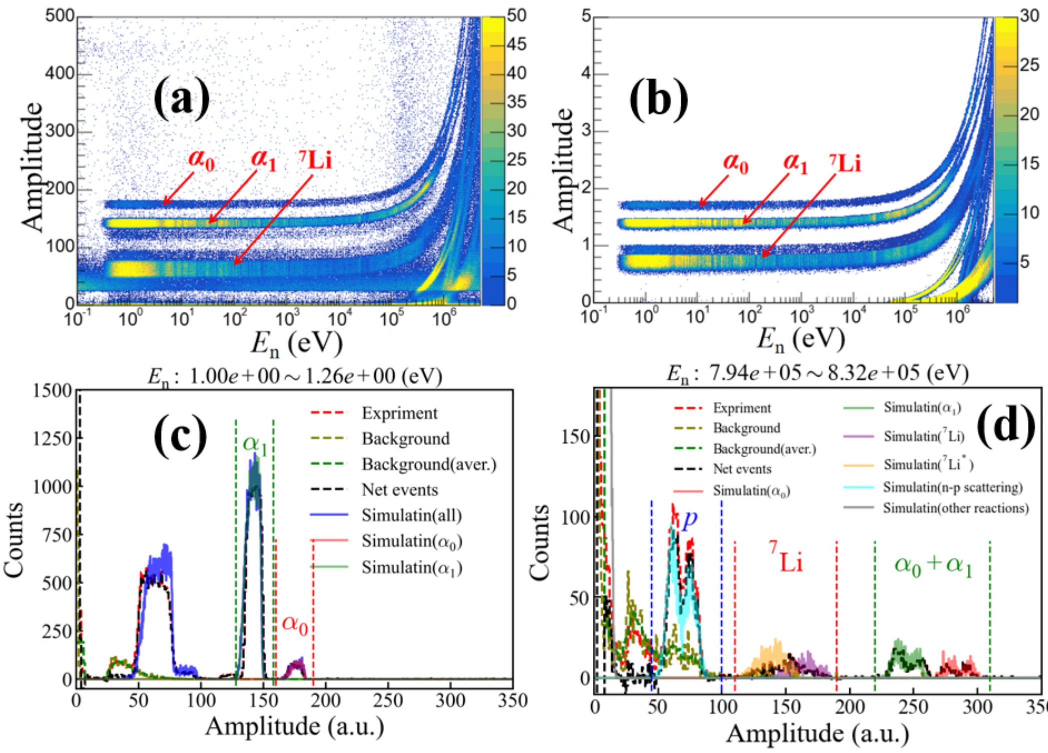

Fig. 4. (color online) Measured E_n-Amplitude two-dimensional spectrum at the angle position of 30.1° (a), simulated E_n-Amplitude two-dimensional spectrum at the angle position of 30.1° (b), experimental PHS and simulated PHS in the neutron energy bin from 1.00 eV to 1.26 eV (c) and from 794 keV to 832 keV (d) at 30.1°.

^{10}B(n, α_0)^{7}Li , ^{10}B(n, α_1)^{7}Li*, ^{10}B(n, p) (Q = 0.23 MeV), ^{10}B(n, $t2\alpha$) (Q = 0.322 MeV), ^{10}B(n, n)^{10}B, n-p scattering, and ^{27}Al (n, α)^{24}Na (Q = –3.132 MeV) reactions. The evaluated values of the cross sections and angular distributions from the ENDF/B-VIII.1 library [21] were used during the simulations. Additionally, the double-bunch proton mode with an interval of 410 ns and the ~70 ns proton pulse width were considered. The simulation result shown in Fig. 4(b) indicates that the ^{7}Li and background events from other reactions (such as ^{10}B(n, p), n-p scattering, *etc.*) rarely interfere with the α_0 and α_1 events for E_n below 3.0 MeV. The α_0 and α_1 events could be clearly distinguished in the neutron energy region below 1 MeV. However, above this energy region, both the α_0 and α_1 events originating from the double-bunch proton pulses gradually separate, resulting in the overlap of α_0 and α_1 events.

The pulse height spectra (PHSs) at different E_n bins were obtained to determine the $N_\alpha(E_n, \theta_{\rm lab})$ counts. For E_n < 100 keV, because the kinetic energies of the emitted α particles remained nearly constant, the measured and simulated PHSs at 10 neutron energy bins per decade (bpd) were obtained, one of which is shown in Fig. 4(c). For E_n > 100 keV, to enhance the energy resolution, PHSs at 50 bpd were constructed to determine the counts of a events and to subtract the background. One of the PHSs at 50 bpd is shown in Fig. 4(d). These counts were subsequently re-binned to 10 bpd to derive differential cross sections.

The background from both the strong gamma flash and the backing sheet is non-negligible, so background measurement and subtraction are essential. The measured PHSs of the foreground spectra are represented in Figs. 4(c) and (d) as red dashed lines, whereas the corresponding background spectra are represened by yellow dashed lines. The neutron fluences were normalized between the background and the ^{10}B(n, α)^{7}Li measurement by integrating the accelerator proton flux. The experimental background PHSs were smoothed before obtaining the background-subtracted (net) PHSs, with the smoothed background spectra represented by the green dashed lines in Figs. 4(c) and (d). The resulting net spectra are indicated by the black dashed lines in Figs. 4(c) and (d). To identify the ^{10}B(n, α)^{7}Li, ^{10}B(n, α_0)^{7}Li, and ^{10}B(n, α_1)^{7}Li* events, the background-subtracted PHSs were compared with the simulated results, which are represented by the blue, red, and green solid lines in Figs. 4(c) and (d). The results indicate that the simulated PHSs agree with the measured PHSs. These simulations also enabled the determination of the detection efficiencies at various angle positions. In addition, the contribution of ambient-scattered thermal neutrons to the background is negligible, due to the their very low flux (< 10 /cm^2/s) [22].

At detection angles greater than 30.0°, the impact of the background on the α event was very small. Considering that the background was smoothed, one fifth of the background counts was considered to be error, and the uncertainty from background subtraction was less than 1%. At the smallest detection angle (20.1°), the background interference was more significant, because the Si detection was near the neutron beam. The uncertainty from the background subtraction for the ^{10}B(n, α_0)^{7}Li events reached 20% only in a few energy bins above 100 keV, whereas in most energy bins, it remained below 1%. Furthermore, the uncertainty of determination of the valid area for the ^{10}B(n, α)^{7}Li and ^{10}B(n, α_1)^{7}Li* events was estimated to be less than 1% in the neutron energy region below 300 keV and less than 3% in the region from 300 keV to 1 MeV. For the ^{10}B(n, α_0)^{7}Li events, the uncertainty of determination of the valid area could reach up to 17.5% only in a few energy bins above 300 keV, whereas in most energy bins, it remained below 4%. In several energy bins above 300 keV, the statistical errors and the the uncertainty of the background subtraction for ^{10}B(n, α_0)^{7}Li events were significant, owing to low counts of ^{10}B(n, α_0)^{7}Li events and high background counts. The detection efficiency at each detection angle was found to be approximately 100%.

Owing to the 410 ns interval between the double-bunch proton beams, there is a non-negligible error in the determination of neutron energies above 0.02 MeV. For E_n < 3.0 MeV, since there is no dense resonance structure in the ^{10}B(n, α)^{7}Li, ^{10}B(n, α_0)^{7}Li, and ^{10}B(n, α_1)^{7}Li* cross sections, an iterative method was used for unfolding. This unfolding method has been successfully used in our previous measurements of the ^{6}Li(n, t)^{4}He and ^{10}B(n, α)^{7}Li reactions at the CSNS Back-n white neutron source [7,12]. Although the double-bunch unfolding effectively reduces neutron energy deviation, it is the most significant source of uncertainty of the measured differential and angle-integrated cross sections. The deviation before and after the double-bunch unfolding is regarded as the error of the double-bunch unfolding. For differential cross sections, the uncertainty introduced from the unfolding process ranges from 0.2% to 19.8%, whereas for angle-integrated cross sections, the uncertainty ranges from 0.2% to 2.3%. A summary of the uncertainty can be found in Sec. C.

B. Determination of the relative neutron fluence

The ^{6}Li-Si monitor [17] was used to measure the neutron flux. The relative neutron fluence $I(E_n)$ was calculated as follows:

$$I(E_n)=\varepsilon_{\rm nor}\frac{N(E_n)}{\dfrac{{\rm d}\sigma}{{\rm d}\Omega}(E_n,\theta_{\rm lab}=135^{\rm o})\cdot\Delta\Omega\cdot N_{\rm s}}, \qquad (2)$$

where $N(E_n)$ is the ^{6}Li(n, t)^{4}He event number in each neutron energy bin, and $\dfrac{{\rm d}\sigma}{{\rm d}\Omega}(E_n, \theta_{\rm lab} = 135°)$ is the differential cross sections of the ^{6}Li(n, t)^{4}He reaction determined using the evaluation data obtained form ENDF/B-VIII.1 [21], JEFF-3.3 [23], and BROND-3.1 [24]. $\Delta\Omega$ is the solid angle of the silicon detector, and $N_{\rm s}$ is the relative ^{6}Li atom number in the ^{6}LiF sample. $N_{\rm s}$ was presented in Sec. II.C, and $\Delta\Omega$ was obtained by Monte Carlo simulations using Geant4 code [19]. Consistent with Eq. (1), the same normalization factor ($\varepsilon_{\rm nor}$) was used here.

The signals from five silicon detectors, positioned at the same receiving angle of 135° with respect to the ^{6}LiF sample in the laboratory system (as described in Sec. II.C), were merged and analyzed to enhance the statistical accuracy of the neutron fluence. The E_n-Amplitude two-dimensional spectrum measured by the ^{6}Li-Si monitor after merging is shown in Fig. 5(a), where the triton and α events from the ^{6}Li(n, t)^{4}He reaction are clearly separated at E_n < 3.0 MeV. The simulated E_n-Amplitude two-dimensional spectrum is shown in Fig. 5(b). When the neutron energy is below 3.0 MeV, the valid-event-area of the triton and α events from the ^{6}Li(n, t)^{4}He reaction can be clearly identified, and the influence of the background is negligible. The primary background sources include neutron-induced reactions from the aluminum backing (*e.g.*, ^{27}Al(n, p)^{27}Mg (Q = −1.828 MeV), ^{27}Al (n, α)^{24}Na (Q = −3.132 MeV), and ^{19}F(n, α)^{16}N (Q = −1.525 MeV) reactions) and the gamma-flash. The gamma-flash effects are minimal owing to the large angle placement of the detectors, and the background contributions from the aluminum backing are significant only for E_n > 3.0 MeV.

To obtain the triton and α count at an energy bin and to determine their detection efficiencies, the experimental PHSs with 10 neutron bins per decade (10 bpd) were compared with the simulated results. A typical experimental PHS at E_n < 100 keV is shown in Fig. 5(c), compared with the simulated PHS. The detector efficiency for triton and α events in the neutron energy below 100 keV is nearly 100% based on the simulation data. For E_n < 100 keV, the uncertainty of determination for the valid area and the detector efficiency is less than 0.5%, and the statistical uncertainty of the triton and α events is less than 1.0%. The triton and alpha count spectra from the double-bunch neutron were unfolded using the iterative method, which is the same method used for the analysis of the ^{10}B data in Sec. III.A. The uncertainty calculation is the same as in Sec. III.A, and the uncertainty introduced from the double-brunch unfolding is less than 1.6%.

The differential cross sections of the ^{6}Li(n, t)^{4}He reaction for different neutron energies were taken from the average of the evaluation data for ENDF/B-VIII.1 [21], JEFF-3.3 [23], and BROND-3.1 [24]. The uncertainties

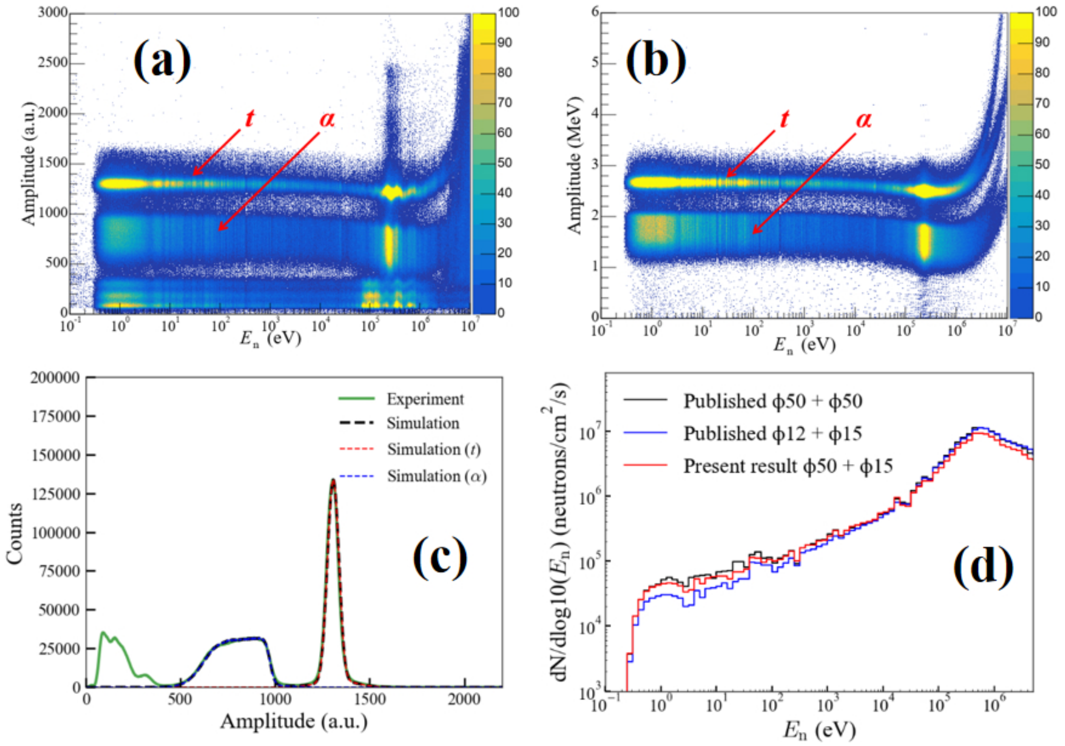

Fig. 5. (color online) Measured E_n-Amplitude two-dimensional spectrum of the ^{6}Li-Si monitor (a), simulated E_n-Amplitude two-dimensional spectrum (b), experimental and simulated PHSs at neutron energies below 100 keV (c), and measured neutron flux with 10 bpd [24, 25] (d).

of the evaluation data were estimated from the maximum deviation among different datasets. The uncertainties of the evaluated differential cross sections for both triton and α emissions at $\theta_{\rm lab}$ = 135° were less than 0.5% for neutron energies below 1 keV. In the neutron energy range from 1 keV to 100 keV, the uncertainties of the evaluated differential cross sections for triton emission increase from 0.5% to 3.2%, and those for α emission increase from 0.5% to 1.4%. $\varepsilon_{\rm nor}$ was calculated using the neutron flux in the neutron energy from 0.5 eV to 1.5 MeV with a beam configuration of Ø50 mm (shutter) + Ø50 mm (collimator 1) published in 2024 [25, 26], with a normalization uncertainty of ~1.3%. In the energy range from 0.3 eV to 100 keV, the neutron flux was calculated using both the counts of triton and α events from Fig. 5(a), according to Eq. (2). The neutron fluxes derived from triton and α events show a discrepancy of less than 3.0%. To address the constraint of relying solely on the differential cross sections from a single angle position, a statistically weighted average of the two neutron fluxes derived independently from triton and α events was employed, with weights determined by their event statistics. The resulting flux was used in Eq. (1), and the uncertainty values ranged from 1.5% to 2.6% for the determination of the differential cross sections of the ^{10}B(n, α)^{7}Li reaction.

The pronounced resonance at approximately 0.24 MeV in the excitation function of the ^{6}Li(n, t)^{4}He reaction renders this reaction unsuitable for direct neutron flux measurements at neutron energies above 100 keV. In the neutron energy range from 100 keV to 3.0 MeV, the neutron flux was derived by normalizing this parameter for the Ø50 mm + Ø50 mm configuration to the integral of the flux measured by the ^{6}Li-Si monitor. The final uncertainty was obtained by combining the contributions from published data and the normalization process and ranged from 1.8% to 2.7%. The measured neutron flux using the ^{6}Li-Si monitor is represented by the red line in Fig. 5(d). The black line in Fig. 5(d) indicates the published neutron flux data obtained with a beam configuration of Ø50 mm (shutter) + Ø50 mm (collimator 1), whereas the blue line corresponds to the configuration of Ø12 mm (shutter) + Ø15 mm (collimator 1). Compared with the Ø50 mm + Ø50 mm configuration, the neutron flux measured with Ø12 mm + Ø15 mm differs more significantly from that of the Ø50 mm + Ø15 mm configuration of the present experiment.

C. Calculation of the differential cross sections and angle-integrated cross sections

According to Eq. (1), the relative differential cross sections were obtained and subsequently fitted using fourth-order Legendre polynomial series. The fitted functions were then integrated to yield the relative angle-in-

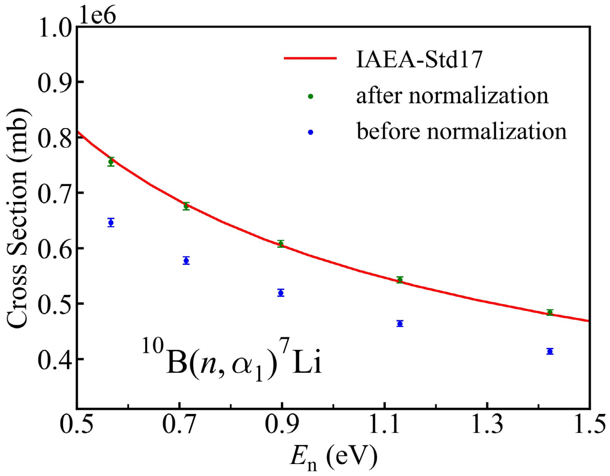

Fig. 6. (color online) The determination of the normalization factor.

tegrated cross sections. As shown in Fig. 6, the relative angle-integrated cross sections for the $^{10}B(n, \alpha_1)^7Li^*$ reaction (the blue points) were normalized to the standard cross section (angle-integrated cross sections) from IAEA-Std17 [3] in the neutron energy range from 0.5 eV to 1.5 eV. This procedure was used to determine the normalization factor ε_{nor} of the present work for both the angle-integrated and differential cross sections.

The uncertainty of this normalization factor is 1.3%, which accounts for both the uncertainty of the standard cross section and the deviation of cross sections between the normalized results and evaluated values. Table 2 details the sources of the uncertainties and their magnitudes.

The sources of uncertainties for the differential cross sections of the $^{10}B(n, \alpha_1)^7Li^*$,$^{10}B(n, \alpha_0)^7Li$, and $^{10}B(n, \alpha)^7Li$ reactions include the uncertainties of the counts of events, relative neutron flux, detection solid angles, number of ^{10}B atoms, and normalization factor. Among these, the uncertainties of the counts of the $^{10}B(n, \alpha_1)^7Li^*$,$^{10}B(n, \alpha_0)^7Li$, and $^{10}B(n, \alpha)^7Li$ reactions arise from the uncertainties in the statistical error of the valid α events, the unfolding of the double-bunch proton beams, the determination of the valid-even-area, the background subtraction, and the detection efficiency. For the differential cross sections of the $^{10}B(n, \alpha)$ ^7Li and $^{10}B(n, \alpha_1)^7Li^*$ reactions, the total uncertainty ranges from 2.4% to 8.7%. For the $^{10}B(n, \alpha_0)^7Li$ reaction, the uncertainty ranges from 3.3% to 32.7%, which is mainly because the counts of the $^{10}B(n, \alpha_0)^7Li$ reaction are significantly less than those of the $^{10}B(n, \alpha)$ ^7Li and $^{10}B(n, \alpha_1)^7Li^*$ reactions. In the neutron energy range below 1 keV, the uncertainties of the differential cross sections for the $^{10}B(n, \alpha)$ ^7Li and $^{10}B(n, \alpha_1)^7Li^*$ reactions primarily originate from the uncertainties in normalization, nuclear number, and neutron flux measurements. In contrast, at high neutron energies, statistical errors and double-bunch unfolding errors are the primary sources of uncertainties. For the $^{10}B(n, \alpha_0)^7Li$ reaction, the uncertainties due to statistical errors, double-bunch unfolding, determination of the valid-even-area, and background subtraction are larger than those of $^0B(n, \alpha)$ ^7Li and $^{10}B(n, \alpha_1)^7Li^*$ reactions. The complete differential cross section data of the present study are provided in the Supporting Information file "Differential cross sections.xlsx".

For the angle-integrated cross sections, the uncertainties owing to the statistical errors, double-bunch unfold-

Table 2. Sources of uncertainties and their magnitudes.

Source of uncertainty	Magnitude (%)	
	Differential cross sections	Angle-integrated cross sections
Relative neutron flux	1.5−3.0	1.5−3.0
Statistical error of the valid α events	0.5−5.5^a (10.7^b)	0.2−2.6
Unfolding of the double-bunch proton beams	0.5−5.6^a (18.5^b)	0.2−2.8
Determination of the valid-even-area	< 4.0^a (< 17.5^b)	< 0.6^a (< 3.0^b)
Background subtraction	< 5.0^a (< 22.8^b)	< 0.1^a (< 1.5^b)
Detection efficiency	< 0.1	< 0.1
Number of ^{10}B atoms	1.0	1.0
Detection solid angle	< 0.4	< 0.4
Legendre polynomial fitting	-	0.2−6.2
Normalization	1.3	1.3
Total uncertainty of the $^{10}B(n, \alpha)$ ^7Li reaction	2.4−8.5	2.4−7.0
Total uncertainty of the $^{10}B(n, \alpha_0)$ ^7Li reaction	3.3−32.7	3.3−7.9
Total uncertainty of the $^{10}B(n, \alpha_1)$ ^7Li reaction	2.4−8.7	2.4−6.4

a: uncertainties of the $^{10}B(n, \alpha)$ ^7Li and $^{10}B(n, \alpha_1)$ $^7Li^*$ reactions. b: uncertainties of the $^{10}B(n, \alpha_0)$ ^7Li reaction.

ing, determination of the valid-even-area, and background subtraction are significantly reduced, whereas an additional uncertainty component is introduced by the Legendre polynomial fitting. For the angle-integrated cross sections of the ^{10}B(n, α) ^{7}Li and ^{10}B(n, α_1)^{7}Li* reactions, the total uncertainty ranges from 2.4% to 7.0%. For the ^{10}B(n, α_0)^{7}Li reaction, the uncertainty ranges from 3.3% to 7.9%. The present experimental data for the angle-integrated cross sections for the ^{10}B(n, α_1)^{7}Li* ,^{10}B(n, α_0)^{7}Li, and ^{10}B(n, α)^{7}Li* reactions are included in the Supporting Information file "Angle-integrated cross sections.xlsx".

IV. RESULT AND DISCUSSIONS

After the data processing presented in Sec. III, the differential cross sections for the ^{10}B(n, α)^{7}Li reaction were obtained from 20.1° to 158.3° (13 angles) in the neutron energy region from 0.3 eV to 3.0 MeV with 10 bpd (70 energy points). The differential cross sections for the ^{10}B(n, α_0)^{7}Li and ^{10}B(n, α_1)^{7}Li* reactions were also obtained at the same angular positions in the neutron energy region from 0.3 eV to 1.0 MeV with 10 bpd (65 energy points). The present differential cross section results are discussed in Sec. IV.A. In addition, the present angle-integrated cross sections for these three reactions were obtained in the corresponding neutron energy range, which are discussed in Sec. IV.B.

A. Differential cross sections

Typical measurement results of differential cross sections for ^{10}B(n, α_1)^{7}Li*,^{10}B(n, α_0)^{7}Li, and ^{10}B(n, α)^{7}Li* reactions are shown in Figs. 7, 8, and 9, respectively. These results are compared with existing data from measurements and evaluations.

In the neutron energy range below 1 keV, the present differential cross sections of these three reactions exhibit a nearly isotropic distribution in the center-of-mass system, consistent with both the evaluations and measurements of Haoyu Jiang (2019) [7]. As shown in Figs. 7(a), 8(a), and 9(a), this agreement confirms the reliability of the present experimental results to an extent. In Fig. 7(a), the differences between the present results (black points) and the previous results (red points) arise from the difference in neutron energy. According to IAEA-Std17 [3], the ^{10}B(n, α_1)^{7}Li* cross section is 540 b at E_n = 1.129±0.004 eV for the present measurement, compared

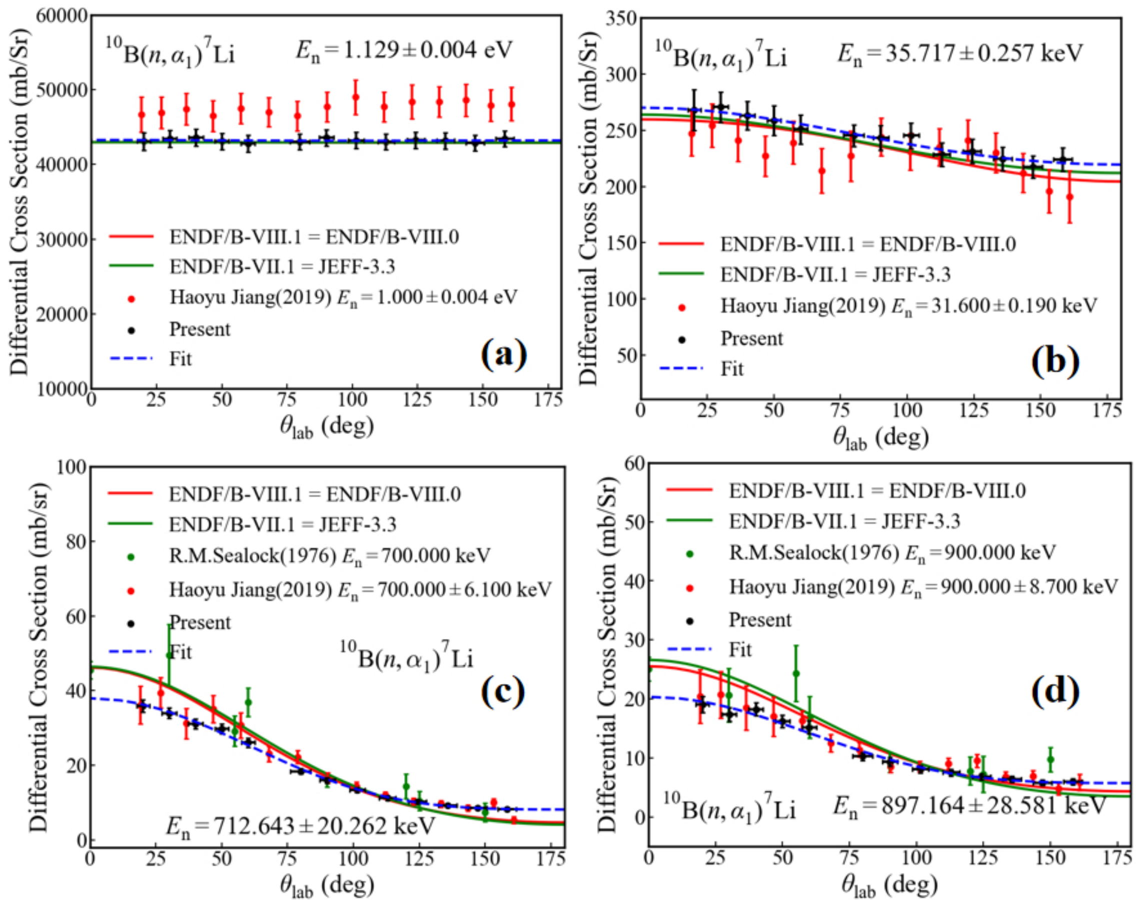

Fig. 7. (color online) Typical differential cross sections of the ^{10}B(n, α_1)^{7}Li* reaction measured in the present study compared with existing results of measurements and evaluations [4, 21, 23, 27, 28].

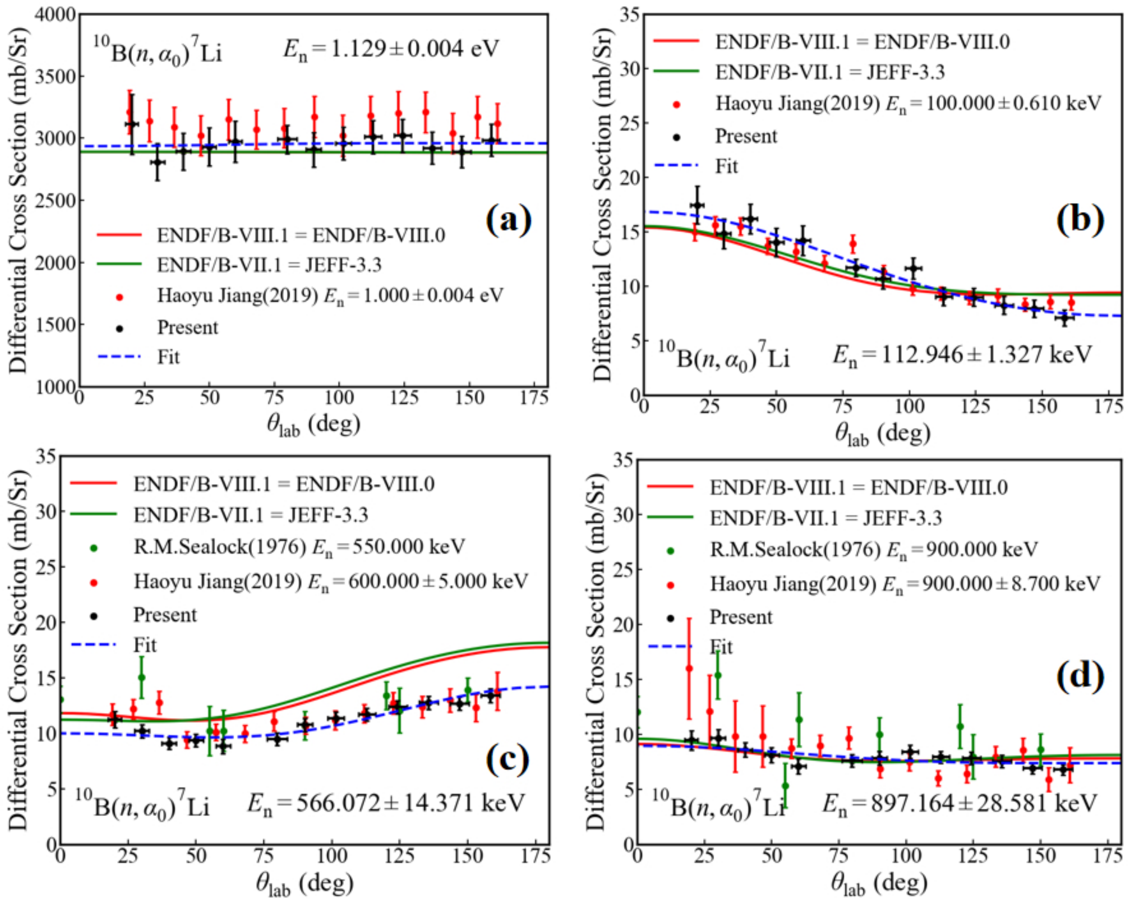

Fig. 8. (color online) Typical differential cross sections of the ^{10}B(n, α_0)^{7}Li reaction measured in the present study compared with existing results of measurements and evaluations [4, 21, 23, 27, 28].

to 573 b at E_n = 1.000±0.004 eV for the previous measurement.

In the neutron energy range from 1 keV to 100 keV, the present differential cross sections of these three reactions exhibit a slight forward bias in the laboratory reference system, due to the effect of nuclear reaction kinetics, as shown in Figs. 7(b) and 9(b). In addition, these results agree well with both the evaluations and measurements.

In the neutron energy range from 100 keV to 1 MeV, the present differential cross sections of the ^{10}B(n, α_1)^{7}Li* reaction display a strong forward bias, which is mainly attributed to the 7/2$^+$ s-wave state of the compound nucleus ^{11}B [30], as shown in Figs. 7(c) and 7(d). Compared with existing measurements, the present results are consistent with the measurement data of Haoyu Jiang (2019) [7]. However, noticeable discrepancies are observed between the present data and the measurement data of R.M.Sealock (1974) [5]. Compared with the evaluations, the present results show a similar forward trend, with smaller magnitudes than those predicted in the evaluation libraries including ENDF/B-VIII.1 [21] and JEFF-3.3 [23]. For the ^{10}B(n, α_0)^{7}Li reaction, the present differential cross sections show a strong backward bias in the 0.3−0.6 MeV region, which is attributed to the 5/2$^-$ p-wave (E_n ~ 0.52 MeV) resonance of the compound nucleus ^{11}B [30], as shown in Fig. 8(c). In the 0.6−1.0 MeV region, the present differential cross sections of the ^{10}B(n, α_0)^{7}Li reaction exhibit a nearly isotropic distribution in the laboratory system, as shown in Fig. 8(d). Compared with the measurement results, the present results are consistent with the measurement data of Haoyu Jiang (2019) [7] and are lower than those of R.M.Sealock (1974) [5] at small angles.

In the neutron energy range of 1.0−3.0 MeV, the present differential cross sections of the ^{10}B(n, α)^{7}Li reaction exhibit a forward peak, which might be attributed to the resonances of the 9/2$^-$ p-wave state (E_n = 1.83 MeV) and 5/2$^+$ or 7/2$^+$ d-wave state (E_n = 1.88 MeV) of the compound nucleus ^{11}B [32], as shown in Figs. 9(c) and 9(d). Compared with the data from evaluations, the present results deviate from the evaluated trends in the ENDF/B-VIII.1 [21] and CENDL-3.2 [27] libraries, where the differential cross sections decrease monotonically with increasing emission angle. The experimental results are in best agreement with the ENDF/B-VIII.1 data [21] among all the evaluated nuclear data libraries.

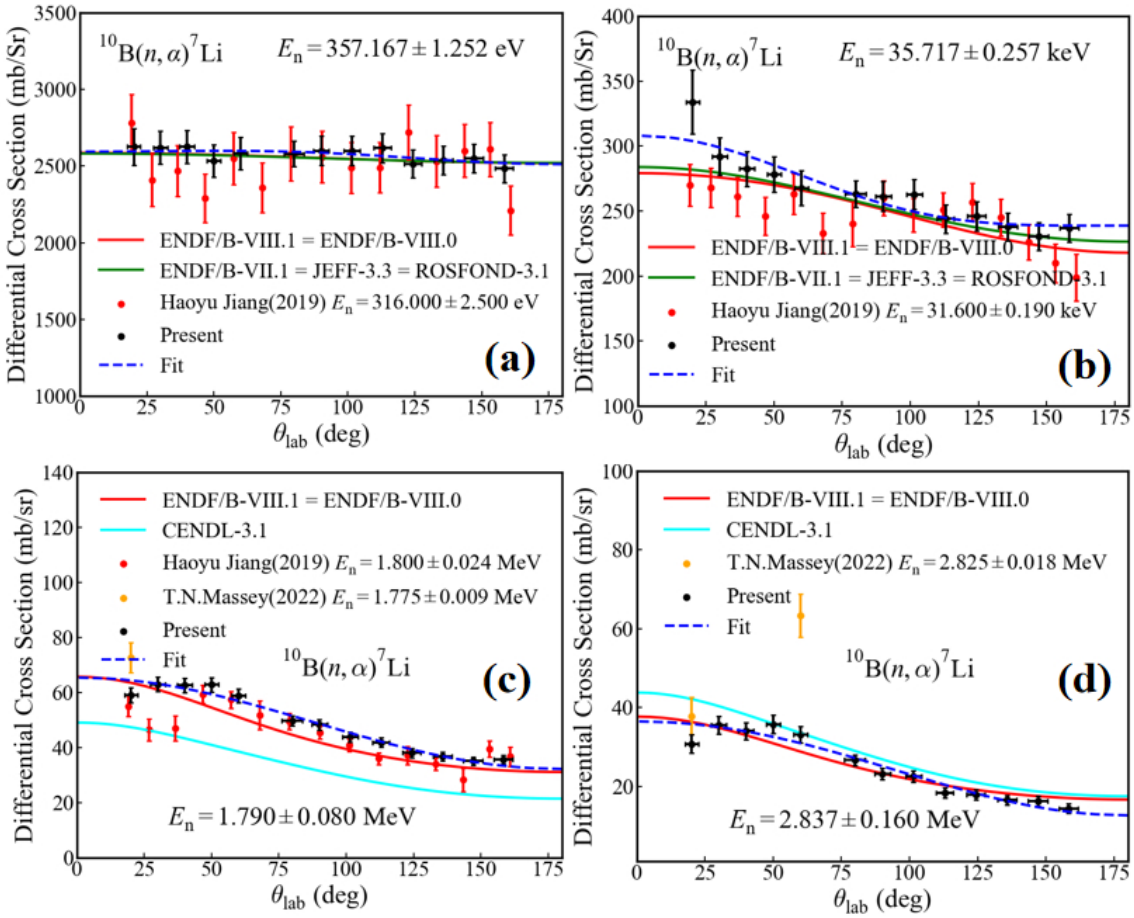

Fig. 9. (color online) Typical differential cross sections of the ^{10}B(n, α)^{7}Li reaction measured in the present work compared with existing results of measurements and evaluations [4, 21, 23, 27, 28].

In comparison with previous measurements, the present differential cross sections of the ^{10}B(n, α)^{7}Li reaction at 30.1° and 40.0° are significantly higher than those reported by Jiang (2019) [7], as shown in Fig. 9(c). This might be due to the excessive background noise in the experiments by Jiang (2019) [7]. Compared with the results of T.N. Massey (2022) [8], the present data have lower values at the forward emission angles, as shown in Fig. 9(d).

In general, the present differential cross sections are consistent with the evaluation data. Compared with existing measurement results of the differential cross sections for the ^{10}B(n, α_1)^{7}Li* ,^{10}B(n, α_0)^{7}Li, and ^{10}B(n, α)^{7}Li reactions available in the EXFOR library [4], the present results are in good overall agreement with those reported by Haoyu Jiang (2019) [7]. In comparison, the present results exhibit a more systematic behavior and smaller uncertainties, particularly for the ^{10}B(n, α_0)^{7}Li reaction, owing to improved statistics.

B. Angle-integrated cross sections

The present results of angle-integrated cross sections for the ^{10}B(n, α_1)^{7}Li* ,^{10}B(n, α_0)^{7}Li, and ^{10}B(n, α)^{7}Li reactions are shown in Figs. 10, 11, and 12, which are compared with existing measurements and evaluation results. The inset in the upper right corner of these three figures shows enlarged views in the 0.1−3.0 MeV region. The present results are in good agreement with the findings from evaluation libraries, including ENDF/B-VIII.1 [21], ENDF/B-VII.1 [28], JEFF-3.3 [23], ROSFOND-3.1 [24], CENDL-3.2 [27], and JENDL-5.0 [29].

In the neutron energy range from 0.3 eV to 100 keV, where the excitation functions of these three reactions follow the 1/v law, the present angle-integrated cross sections agree well with the evaluation results. In this energy region, given that the s-wave states of α_1 partial ($\Gamma_{n(\mathrm{C.M.})}$ = 0.77 MeV and $\Gamma_{\alpha(\mathrm{C.M.})}$ = 0.113 MeV) have a larger width compared with the α_0 partial width ($\Gamma_{\alpha(\mathrm{C.M.})}$ = 0.001 MeV) [30], the cross sections of the ^{10}B(n, α_1)^{7}Li* reaction are much larger than those of the ^{10}B(n, α_0)^{7}Li reaction. Compared with the results of Haoyu Jiang (2019) [7], the present cross sections do not exhibit oscillations as a function of the neutron energy and have smaller uncertainties because the energy spectrum was measured using the ^{6}Li-Si monitor instead of the ^{235}U(n, f) reaction. Compared with the results of Haoyu Jiang (2019) [7], the present uncertainties of the cross sections are re-

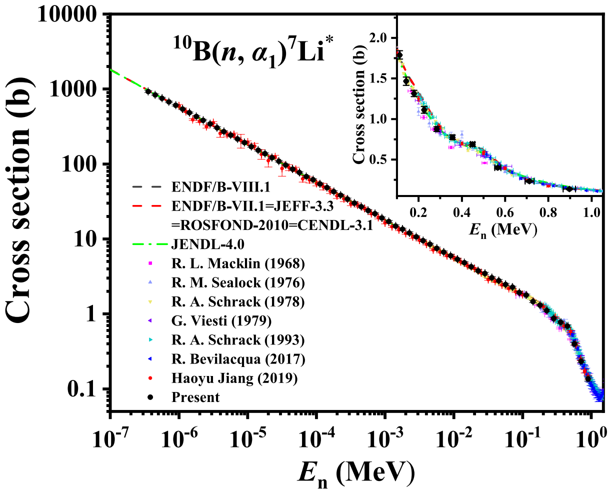

Fig. 10. (color online) Angle-integrated cross sections of the ^{10}B(n, α_1)^{7}Li* reaction compared with existing results of evaluations and measurements [4, 21, 23, 24, 27–29].

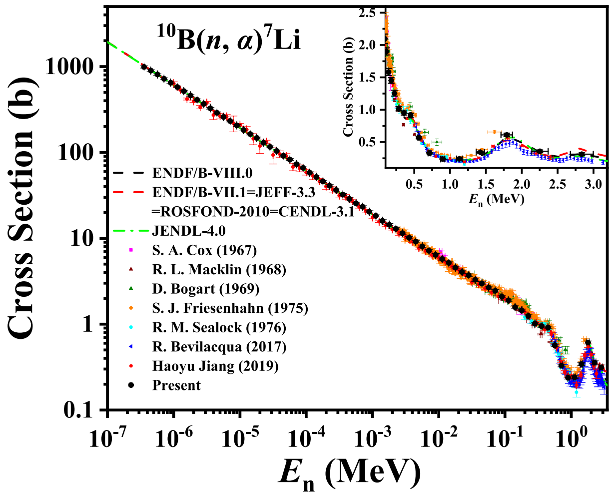

Fig. 12. (color online) Angle-integrated cross sections of the ^{10}B(n, α)^{7}Li reaction compared with existing results of evaluations and measurements [4, 21, 23, 24, 27–29].

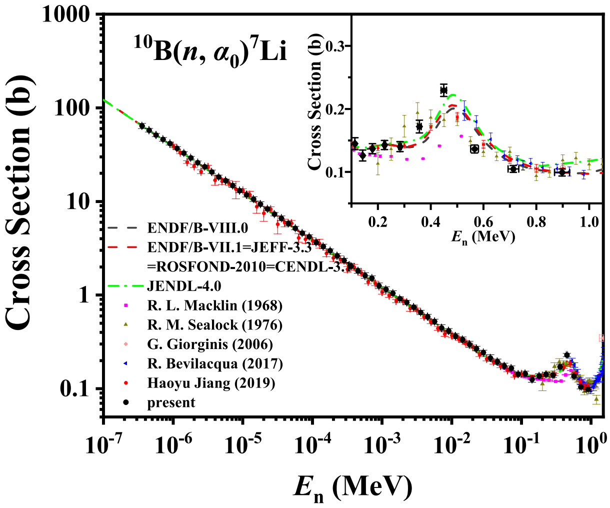

Fig. 11. (color online) Angle-integrated cross sections of the ^{10}B(n, α_0)^{7}Li reaction compared with existing results of evaluations and measurements [4, 21, 23, 24, 27–29].

duced from 2.2%−21.6% to 2.0%−7.6%. In the experiment of Haoyu Jiang (2019) [7], the neutron energy spectrum was measured using a multi-layer fission chamber, which is based on the cross section data of the ^{235}U(n, f) reaction [12]. The cross sections of the ^{235}U(n, f) reaction exhibit dense resonance structures in the neutron energy region below 100 keV. On the contrary, the cross sections of the ^{6}Li(n, t)^{4}He reaction follow a $1/v$ law without significant resonance structures in the same neutron energy range. Thus, in the neutron energy region below 100 keV, the uncertainties of the present neutron energy spectrum measured using the ^{6}Li-Si monitor are smaller.

In the neutron energy region from 100 keV to 1 MeV, the excitation functions of these three reactions do not follow the $1/v$ law. In the 0.5−1.0 MeV, the angle-integrated cross sections of the ^{10}B(n, α_1)^{7}Li* and ^{10}B(n, α)^{7}Li reactions exhibit a rapid decline, as shown in Figs. 10 and 12. Conversely, the angle-integrated cross sections of the ^{10}B(n, α_0)^{7}Li cross section have a resonance peak in the 300 keV – 600 keV region, due to the effect of 5/2$^-$ p-wave (E_n ~ 0.52 MeV) resonance [30], as shown in Fig. 11. This resonance state significantly increases the ^{10}B(n, α_0)^{7}Li cross sections and leads to a rapid decrease in the ^{10}B(n, α_1)^{7}Li* cross sections above 500 keV. The angle-integrated cross sections of the ^{10}B(n, α_1)^{7}Li* and ^{10}B(n, α)^{7}Li reactions are consistent with the evaluation data. However, the present angle-integrated cross sections of the ^{10}B(n, α_0)^{7}Li reaction are higher at $E_n < 0.5$ MeV and lower at $E_n > 0.5$ MeV than the evaluations and other measurements. Compared with existing measurement data, the present cross section data of the ^{10}B(n, α)^{7}Li reaction are closer to the results of Haoyu Jiang (2019) [7] and lower than those of Friesenhahn (1975) [31].

In the neutron energy region from 1.0 MeV to 3.0 MeV, the present results show the resonance effect in the excitation function of the ^{10}B(n, α)^{7}Li reaction near E_n ~ 1.8 MeV, which might be attributed to the 9/2$^-$ p-wave state (E_n = 1.83 MeV) and 5/2$^+$ or 7/2$^+$ d-wave state (E_n = 1.88 MeV) of the compound nucleus ^{11}B [32], as shown in Fig. 12. The angle-integrated cross sections of the ^{10}B(n, α)^{7}Li reaction were consistent with the results of Haoyu Jiang (2019) [7] and the evaluations. Moreover, they were lower than those of Friesenhahn (1975) [31] and higher than those of Hausladen (2017) [33].

V. CONCLUSIONS

In the present study, differential cross sections of the ^{10}B(n, α)^{7}Li reaction were measured using an LPDA detector system at 13 angles from 20.1° to 158.3° in the neutron energy range from 0.3 eV to 3.0 MeV with 10 bpd (70 energy points). Differential cross sections of the ^{10}B(n, α_0)^{7}Li and ^{10}B(n, α_1)^{7}Li* reactions were also measured at the same angular positions in the neutron energy region from 0.3 eV to 1.0 MeV with 10 bpd (65 energy points). Using Legendre polynomial series fitting and integration, the angle-integrated cross sections of these three reactions were obtained in the corresponding neutron energy region. In the neutron energy region from 0.3 eV to 100 keV, the differential cross sections of the ^{10}B(n, α_1)^{7}Li*, ^{10}B(n, α_0)^{7}Li, and ^{10}B(n, α)^{7}Li reactions exhibited a nearly isotropic distribution in the center-of-mass system, and a slight forward bias emerged in the laboratory system as the neutron energy increased. In the neutron energy region from 300 keV to 600 keV, the present differential cross sections of the ^{10}B(n, α_0)^{7}Li reaction exhibited a strong backward trend, consistent with our previous results (Haoyu Jiang, 2019). In the neutron energy region from 100 keV to 1 MeV, the forward trend of the ^{10}B(n, α_1)^{7}Li* differential cross sections in the present result is weaker than that in the evaluations, which also agree with our previous measurement results (Haoyu Jiang, 2019). In the neutron energy from 1.0 MeV to 3.0 MeV, the present differential cross sections of the ^{10}B(n, α_0)^{7}Li reaction exhibit significant forward-peak shape. The present angle-integrated cross sections of these three reactions generally agree with most of the results of evaluations and previous measurements, with minor deviations noted for the ^{10}B(n, α_0)^{7}Li reaction from 0.3 to 0.6 MeV. Compared with other measurement results, the present results have lower uncertainties in the neutron energy region from 0.3 eV to 100 keV. Compared with our previous measurement results (Haoyu Jiang, 2019), the present results have been improved by resolving the issues of the energy spectrum oscillation in the low-energy region, improving measurement statistics, and expanding the measured energy range.

ACKNOWLEDGEMENT

The staff of the Back-n white neutron source facility (https://cstr.cn/31113.02.CSNS.Back-n) at China Spallation Neutron Source (CSNS) are acknowledged for providing a stable neutron beam and technical support.

References

[1] R. Bevilacqua, F. J. Hambsch, R. Bencardino *et al.*, Nucl. Data Sheets **119**, 104 (2014).

[2] F. J. Hambsch and I. Ruskov, Nucl. Sci. Eng. **163**, 1 (2009).

[3] A. D. Carlson, V. G. Pronyaev, R. Capote *et al.*, Nucl. Data Sheets **148**, 143 (2018).

[4] V. V. Zerkin and B. Pritychenko, Nucl. Instrum. Meth. Phys. Res. A **888**, 31 (2018).

[5] R. M. Sealock and J. C, Phys. Rev. C **13**, 2149 (1976).

[6] M. L. Stelts, R. E. Chrien, C. M. McCullagh *et al.*, Phys. Rev. C **19**, 1159 (1979).

[7] H. Jiang, W. Jiang, H. Y. Bai *et al.*, Chin. Phys. C **43**, 124002 (2019).

[8] T. N. Massey, J. E. O'Donnell, J. Ralston *et al.*, Phys. Rev. C **105**, 054612 (2022).

[9] H. Chen and X. L. Wang, Nature Mater **15**, 689 (2016).

[10] J. Y. Tang, Q. An, J. B. Bai *et al.*, Nucl. Sci. Tech. **32**, 11 (2021).

[11] Q. An *et al.* , J. Inst. 12, P07022 (2017).

[12] H. Y. Bai, R. R. Fan, H. Y. Jiang *et al.*, Chin. Phys. C **44**, 014003 (2020).

[13] J. Liu, H. Y. Bai, H. Y. Jiang *et al.*, Eur. Phys. J. A **59**, 106 (2023).

[14] H. T. Jing, J. Y. Tang, H. Q. Tang *et al.*, Nucl. Instrum. Meth. Phys. Res. A **621**, 91 (2010).

[15] L. Y. Zhang *et al.*, Applied Radiation and Isotopes **132**, 212 (2018).

[16] H. Yi, T. F. Wang, Y. Li, *et al.* , J. Inst. **15**, P03026 (2020).

[17] Q. Li, G. Luan, J. Bao *et al.*, Nucl. Instrum. Meth. Phys. Res. A **946**, 162497 (2019).

[18] K. Sun, G. Zhang, H. Yi *et al.*, J. Inst. **18**, P04004 (2023).

[19] S. Agostinelli, J. Allison, K. Amako *et al.*, Nucl. Instrum. Meth. Phys. Res. A **506**, 250 (2003).

[20] B. He, P. Cao, D. L. Zhang *et al.*, Chin. Phys. C **41**, 016104 (2017).

[21] ENDF/B-VIII. 1, https: //www. osti. gov/biblio/2571019. https://doi.org/10.11578/endf/257101922.

[22] Q. Li *et al.*, Nucl. Instrum. Meth. Phys. Res. A **980**, 164506 (2020).

[23] A. J. M. Plompen, O. Cabellos, C. De Saint Jean *et al.*, Eur. Phys. J. A **56**, 181 (2020).

[24] BROND-3.1, https://vant.ippe.ru/en/, reterieved 1st February 2026.

[25] Y. Chen, Y. Qiu, Q. Li *et al.*, Eur. Phys. J. A **60**, 63 (2024).

[26] Y. Chen, G. Luan, J. Bao *et al.*, Eur. Phys. J. A **55**, 115 (2019).

[27] Z. G. Ge, R. R. Xu, H. C. Wu *et al.*, EPJ Web Conf. **239**, 09001 (2020).

[28] M. B. Chadwick *et al.*, Data, Nucl. Data Sheets **112**, 2887 (2011).

[29] O. Iwamoto *et al*, Journal of Nuclear Science and Technology **60**, 1 (2023).

[30] S. L. Hausladen, R. O. Lane, and J. E. Monahan, Phys. Rev. C **5**, 277 (1972).

[31] EXFOR data: https://www-nds.iaea.org/exfor/servlet/X4sGetSubent?reqx=54377&subID=10303004&plus=1,reterieved 1st February 2026.

[32] S. L. Hausladen, C.E. Nelson, and R.O. Lane, Nucl. Phy. A **217**, 563 (1973).

[33] R. Bevilacqua, F. J. Hambsch, M. Vidali *et al.*, EPJ Web Conf. **146**, 11010 (2017)